Full Text View

Volume 29, Issue 5 (May 1999)

Journal of Physical Oceanography
Article: pp. 948–968 | Abstract | PDF (341K)

Frontal Instabilities in a Two-Layer, Primitive Equation Ocean Model

Xiao Bing Shi and Lars Petter Røed

Norwegian Meteorological Institute, Oslo, Norway

(Manuscript received July 31, 1997, in final form June 12, 1998)

DOI: 10.1175/1520-0485(1999)029<0948:FIIATL>2.0.CO;2

ABSTRACT

A linear stability analysis combined with an energy analysis is performed to discriminate between the various instabilities that may develop at upwelling fronts. In the present study, a two-active-layer model of finite depth is considered. Thus, the model includes a variable across-front bottom topography, a sloping interface, a surface elevation, and variable densities in the two layers. In addition, the energy analysis departs from earlier studies in that it makes use of the available gravitational energy to replace the conventional potential energy. The concept of available gravitational energy is akin to available potential energy, but avoids the constraint of considering a closed basin. Interestingly, the earlier findings of two preferred bands of unstable waves are retained in the present model. The first band (wavelengths of 10–30 km) is associated with the so-called frontal instability (frontal mode), and the second band (wavelengths of 60–70 km) is associated with a mixed barotropic–baroclinic instability (mixed mode). The growth rate of the frontal mode is typically in the range of one to two days, while the mixed mode is typically three to five days. Although the frontal mode dominates in most cases, an exception occurs when the horizontal shear (in terms of the jet speed divided by the frontal width) becomes large. Indeed, the frontal mode ceases to exist when the frontal width becomes small enough, depending on the horizontal viscosity. Another exception occurs when the frontal jet is caused by the sloping interface only (no upper-layer density front). In this case the frontal mode is cut off, lending further support to the theory that the smaller-scale waves found in the coastal transition zones of the world oceans indeed owe their presence to the existence of the upwelling front. When the vertical shear is increased, the present analysis reveals that the growth rates of all the unstable waves, in particular the waves associated with the frontal mode, are increased. Moreover, the mixed mode ceases to exist as a preferred band of unstable waves. A final case shows that the frontal mode is unaffected by a sloping bottom topography. This is in support of the suggestion that the frontal mode is trapped to the upper layer. Experiments with a numerical multilayer, primitive-equation ocean model support the findings of the linear stability analysis, both qualitatively and quantitatively. They also reveal a complicated nonlinear wave–wave interaction causing a transition from the well-organized linear instability wave pattern toward a new organized pattern of much longer scale, filament-type, structures.

1. Introduction

In the following, the linearly unstable waves that may grow at an upwelling front are investigated using a linear stability analysis combined with an energy analysis. This subject has recently been treated by Barth (1989a,b;1994), McCreary et al. (1991), Fukamachi et al. (1995), and Young and Chen (1995). The present work extends these studies in that an arbitrarily varying mixed layer depth and surface elevation are included and the density is allowed to vary laterally in both layers.

The study is motivated by investigations revealing the mesoscale structure in the upwelling area off the western Iberian Peninsula (Haynes et al. 1993; Sousa 1995). In the traditional view, upwelling-favorable winds force an offshore (Ekman) transport in the upper ocean, leading to a persistent upwelling of cold and nutrient rich water from below. This causes an upwelling front to be formed offshore that separates the cold saline coastal water from the warmer and fresher ambient water offshore. Such fronts are characterized by sharp lateral gradients in velocity, density, and biological fields and are most commonly observed in eastern ocean boundary regions (Northern Hemisphere) such as the coastal transition zone (CTZ) off the western Iberian Peninsula, the northwestern coast of Africa, and the Oregon and California coasts. An example is provided in Fig. 1, which shows a satellite image of the sea surface temperature off the Iberian Peninsula. This image reveals that the upwelling affects the open ocean due to the formation of large-scale upwelling filaments and squirts, which may reach as far as 200–300 km offshore (Sousa 1995).

Also visible in Fig. 1 are smaller-scale instabilities with wavelengths of approximately 15–30 km. The smaller-scale waves are postulated to be the result of instability mechanisms and are the focus of this study. It is of interest to note that these mesoscale structures are reproducible by numerical models, provided a sufficiently high resolution is used (Stevens et al. 1997).

Of particular relevance to the present study are those of McCreary et al. (1991) and Røed (1996). As for instance revealed by Røed (1996), filaments strikingly similar to those observed off the Atlantic coast of the Iberian Peninsula may be reproduced using a simple 1½-layer model featuring a realistic coastline geometry. Moreover, Feliks and Ghil (1993) studied the evolution of frontal waves using a QG rigid-lid model with several modes in the vertical. They divided the formation of frontal waves into three stages. At first, the evolution is mainly due to linear instability, the second stage is characterized by eddy formation, and finally, eddies grow into filaments that shoot out from the coast.

a. Earlier work

There have been many mathematical and experimental investigations of the dynamics behind upwelling filaments, squirts, and eddies. Whereas the earlier studies used quasigeostrophic (QG) theory, the more recent studies have been based on primitive equation (PE) models. The latter is important since the QG approximation severely restricts the number of possible instability mechanisms. A review of some of the earlier work pertinent to the present study is given by Fukamachi et al. (1995), and only a few comments and remarks are therefore provided here.

In his pioneering study of baroclinic instabilities in a two-layer, constant density, QG model, Phillips (1954) found that the fastest growing, baroclinically unstable waves had the wavelength $\lambda_m = 2\pi R(H_d/H)^{1/4}$, where H and H_d are the thickness of the upper and bottom layers respectively, $R = \{g\Delta\rho HH_d/[f^2\rho_0(H + H_d)]\}^{1/2}$ is the internal Rossby radius of deformation, g is the gravitational acceleration, $\Delta\rho$ is the density difference between the two layers, and ρ_0 is a reference density value. Using values typical for the region off the Iberian Peninsula $\lambda_m \approx 60$ km, which is much longer than the 15–30 km wavelength observed in Fig. 1. It is also substantially shorter than the 100–150 km distance separating the filaments (Haynes et al. 1993; Sousa 1995). Neither of these waves are therefore caused by the mechanism proposed by Phillips (1954). This is to be expected since his theory assumes that the basic state consists of a constant velocity balanced by a linear thickness deviation. When the horizontal density structure of the upper ocean is considered, a new type of unstable wave–frontal instability wave becomes possible, as shown for instance in the more recent studies of Barth (1994), McCreary et al. (1991), and Fukamachi et al. (1995).

As noted by McCreary et al. (1991) and later by Fukamachi et al. (1995), prominent new instability mechanisms can be simulated in PE models that owe their existence to strong lateral density gradients, that is, the existence of a front. This instability is, therefore, called the frontal instability. To avoid confusion regarding terminology, the frontal instability is here defined as being that part of the baroclinic instability that extracts its energy from the basic lateral density gradient and/or density fluctuations.

The work of Young and Chen (1995) is of particular interest. They extended the analysis of Fukamachi et al. (1995) to include a (linearly) varying upper-layer thickness in addition to a variable density in the basic state. They concluded that, when a linear slope in the basic state upper-layer thickness is included, a low wavenumber cutoff exists below which the waves are stable;that is, longer waves are stabilized. In upwelling areas, however, the base of mixed layer is not a linear slope, but exhibits a frontal-like structure. It is therefore of interest to study the case when both the basic upper-layer thickness and density exhibit a frontal structure.

Using a continuously stratified model Barth (1994) investigated the stability of a coastal frontal jet and front and explained the growth of two modes of instability. One is in the longer wavelength band with wavelengths of O(100 km) and extends to the deep ocean. He postulated that this was a modified version of the conventional baroclinic instability. The other mode was in the shorter wavelength band with unstable waves of O(20 km), with a much faster growth rate (e-folding time of 1.5 days). Moreover, another form of instability, inertial instability (Hoskins 1974), can also form if the horizontal velocity shear is larger than the Coriolis parameter f, but in this case the disturbance will not appear as a wavelike instability.

Barth also used results generated with the spectral, nonlinear model of Haidvogel et al. (1991) to study the instability associated with fronts and to compare it with his results obtained using linear instability theory. By imposing the same basic state in the nonlinear numerical model he was able to verify qualitatively the existence of the frontal instability mode by the similarity of the model and the linear instability results.

Fukamachi et al. (1995) analyzed the linearly unstable waves with a 1½-layer model. They obtained two types of instabilities in this model also, confirming the results obtained by Barth (1994). The most unstable waves were in the shorter wavelength band (~ 20 km) and were caused by the frontal instability mechanism. The other instability was in the long wavelength band with wavelengths of about 60 km. These waves were caused by a mixture of barotropic and baroclinic instability and appeared to dominate below a certain threshold of frontal width.

It should be noted that the present model has horizontal density gradients in the layers without having an accompanying vertical shear since it is assumed implicitly that Reynolds stresses balance exactly the z-dependent part of the pressure gradient in the layer model. Criticisms of such models were raised by Young (1994), who argued that momentum is not ensured to be uniformly mixed even though the density can be homogenized by strong vertical mixing processes in the mixed layer. He, nevertheless, developed a partial justification for a model in which the top layer was well mixed in both density and momentum. Later, Young and Chen (1995) found that it was indeed more realistic to include a vertical velocity shear in the mixed layer since the long-wave behavior of the Eady mode can be reproduced nicely this way, and that models with vertical shear make qualitatively different predictions from models without vertical shear under certain circumstances. Therefore, the results from inhomogeneous layer models should be interpreted with care. Nevertheless, such models have not yet failed in any fundamental way to simulate oceanic phenomena, for example, McCreary et al. (1991) and Røed (1996).

b. Present research

The analysis scheme of Fukamachi et al. (1995) is extended below in order to include the effect of bottom topography, that is, a barotropic mode. To this end, a two-active-layer, finite depth model is considered. In the basic state, the interface, the surface, and the density in the upper and lower layers are all allowed to vary in the cross-channel direction and, specifically, to have a (nonlinear) frontal structure. The new scheme also supports lateral density and thickness perturbations in both layers. Thus, the model contains barotropic and frontal instabilities, instability due to vertical velocity shear, inertial instability, as well as a conventional baroclinic instability. An energy analysis along the lines of McCreary et al. (1991) and Fukamachi et al. (1995) is undertaken to investigate the relative importance of the various instability mechanisms present, in which the concept of available gravitation energy of Pinardi and Robinson (1986) and Røed (1997) is used to replace the conventional potential energy.

Six cases are considered. The first is a reference run featuring a flat bottom and a basic-state jet in the upper layer only. This is achieved by letting the basic-state density in the upper layer (baroclinic mode) and the basic-state surface deviation (barotropic mode) vary in such a manner that the lower-layer velocity becomes zero. The basic state has a flat interface and a uniform lower-layer density. Although the reference run is constructed to be similar to the basic state considered by Fukamachi et al. (1995), it differs from theirs in that the basic state necessarily features a barotropic velocity component (due to the finite depth) to make the lower-layer velocity zero. The remaining five cases are sensitivity cases in which the various constraints of the reference run are relaxed. While the first considers the effect of a density front combined with an interface deviation, the second considers the effect of a varying horizontal eddy viscosity; the third the effect of varying the basic-state horizontal shear (essentially the width of the front); the fourth considers the effect of varying the vertical shear, in which case the basic-state lower-layer density is allowed to have a weak front as well; and the fifth and last is constructed to show the effect of introducing a sloping bottom. It should be pointed out that similar sensitivity cases have been carried out by McCreary et al. (1991), Barth (1994), and Fukamachi et al. (1995), however, using different model configurations. Finally, the details and nature of the instabilities are further investigated by comparing the results of the linear instability analysis with the response of a layered, nonlinear, primitive equation numerical model.

The governing equations, including the basic-state balance, the perturbation equations, and the solution method, are presented in section 2. The energy analysis scheme used is presented in section 3. Section 4 gives an account of the results of the linear stability analysis and also includes the results emanating from the energetics applied to the six cases mentioned above. Results from the experiments with the numerical model are discussed in section 5. Finally, section 6 offers a summary and some concluding remarks.

2. The governing equations

The model ocean is a two-active layer, finite depth, primitive equation model with lateral inhomogeneity in the layer densities. As such the model is similar to the reduced-gravity-type models employed by McCreary et al. (1991) and Fukamachi et al. (1995) but, yet, different in that it includes the barotropic mode. For details on the derivation of the model equations the reader is referred to Røed (1995). Let h_i denote the layer thickness, $\mathbf{u}_i$ the depth-averaged layer velocity with components u_i, v_i in the horizontal directions, and ρ_i the depth average layer density. Neglecting the effect of wind forcing, diapycnal mixing, and fluxes across interfaces (including the surface flux) the governing equations become

$$h_{it} + \nabla \cdot (h_i \mathbf{u}_i) = 0, \quad (2)$$

$$(h_i \rho_i)_t + \nabla \cdot (h_i \rho_i \mathbf{u}_i) = \nabla \cdot (h_i \nu_i \nabla \rho_i), \quad (3)$$

where $\mathbf{J}_i$ is the pressure force given by (neglecting surface pressure)

$$\rho_0 \mathbf{J}_i = g\left[\frac{1}{2}\nabla \rho_i h_i^2 + h_i \nabla \sum_{j=1}^{i-1} \rho_j h_j + \rho_i h_i \nabla \sum_{j=i+1}^{N} h_j - \rho_i h_i \nabla D\right]. \quad (4)$$

The water mass is confined within a meridional channel with x pointing eastward (across channel direction) and y pointing northward (along channel), respectively. The layer index i (i = 1, 2) is counted from top down (see Fig. 2). Subscript t indicates differentiation with respect to time, and the ∇ operator denotes a differentiation in the horizontal direction only. The Coriolis parameter is f, ν_i is the eddy viscosity coefficient, ρ_0 is a constant reference density, g is the gravitational acceleration, $\mathbf{k}$ is a unit vector along the upward z axis, and D is the ocean depth. Note that the above equations are valid for an arbitrary number of layers, but for the purpose of this study only two layers are considered.

a. The basic state

The basic state is assumed to be in geostrophic balance and to consist of a frontal jet varying in the cross-channel direction (x axis) only. The frontal area over which the basic-state variables vary is sufficiently remote from the walls to be considered a free jet (e.g., Lee and Csanady 1994), that is, not to be impeded by the presence of the walls. Thus, the frontal area is located at least one Rossby radius away from the walls. Given this constraint, the diffusion of the basic state is small everywhere, even close to the walls, and may consequently be neglected everywhere. Thus, in accordance with (1) the basic state is governed by

$$V_1 = \frac{g}{f\rho_0}\left(R_1 \eta_x + \frac{1}{2} H_1 R_{1x}\right) \quad (5)$$

and

$$V_2 = \frac{g}{f\rho_0}\left[(R_1 H_1)_x + R_2 \zeta_x + \frac{1}{2} H_2 R_{2x}\right], \quad (6)$$

where η is the surface deviation, ζ is the interface depth (Fig. 2), and $V_i(x)$, $H_i(x)$, and $R_i(x)$ denote the velocity, thickness, and density of the basic state respectively. Note that the surface, interface deviations, and the layer thickness of the basic state are interrelated such that

$$\eta = -D + H_1 + H_2 \quad (7)$$

and

$$\zeta = -D + H_2, \quad (8)$$

respectively. Thus, only two of the five can be chosen independently.

b. Perturbation equations

To study the possible instabilities that may grow, the basic state is perturbed as follows:

$$\rho_i = R_i(x) + \rho_i'(x, y, t), \qquad (11)$$

where $\mathbf{u}_i'$, h_i', and ρ_i', are the perturbation waves superimposed on the basic state and **j** is a unit vector along the positive y axis. Assuming that the horizontal diffusion coefficient is constant and equal in the two layers and that the perturbations are small to $O(\varepsilon)$, where ε is an arbitrarily small parameter, (1)–(3) can be linearized to give

$$\mathbf{u}_{it}' + V_i\mathbf{u}_{iy}' + u_i'V_{ix}\mathbf{j} + f\mathbf{k} \times \mathbf{u}_i' + \mathbf{J}_i' = \nu\nabla^2\mathbf{u}_i' \qquad (12)$$

$$\rho_{it}' + V_i\rho_{iy}' + u_i'R_{ix} = \nu\nabla^2\rho_i', \qquad (13)$$

$$h_{it}' + V_ih_{iy}' + H_i\nabla \cdot \mathbf{u}_i' + u_i'H_{ix} = 0. \qquad (14)$$

The $O(\varepsilon)$ pressure gradient fields are given by

$$\rho_0\mathbf{J}_1' = g\left[R_1(\nabla h_1' + \nabla h_2') + \frac{1}{2}H_1\nabla\rho_1' + \frac{1}{2}h_1'\nabla R_1 + \rho_1'\nabla\eta\right], \qquad (15)$$

and

$$\rho_0\mathbf{J}_2' = g\left[\nabla(\rho_1'H_1) + \nabla(R_1h_1') + \frac{1}{2}h_2'\nabla R_2 + \frac{1}{2}H_2\nabla\rho_2' + R_2\nabla h_2' + \rho_2'\nabla\zeta\right], \qquad (16)$$

respectively.

Solutions to the two-dimensional perturbation equations (12)–(14) are sought in the form of normal modes;that is,

$$(\mathbf{u}_i', h_i', \rho_i') = (\hat{\mathbf{u}}_i, \hat{\mathrm{h}}_i, \hat{\boldsymbol{\rho}}_i)e^{i(ly-\sigma t)}, \qquad (17)$$

where $\hat{\mathbf{u}}$, $\hat{\mathrm{h}}$, $\hat{\boldsymbol{\rho}}$ are small amplitude functions of $O(\varepsilon)$ relative to the basic state, and vary in the cross-channel (x axis) direction only, l is an alongfront wavenumber in the channel direction (y axis), and σ is a complex frequency with real and imaginary parts, σ_r and σ_i. Thus, unstable (stable) waves are associated with positive (negative) values of σ_i.

c. Solution method

Substitution of (17) into (12)–(14) gives a coupled set of equations for the amplitude functions (not shown), which are solved numerically. To this end a finite difference grid is constructed with $\mathfrak{v}'$, h', ρ' points located at the center of cells of size Δx and with u' points located at the edges of the cells. At the two channel walls $x = 0, L$ the conditions $u_i' = 0$, $\mathfrak{v}_{ix}' = 0$, and $\rho_{ix}' = 0$ are applied to ensure that neither the momentum nor the heat is transported through the boundaries. The finite difference equations are then reduced to a set of algebraic equations that can be written in matrix form $\mathbf{Ex} = \sigma\mathbf{x}$. The matrix **E** contains the information about the basic state, while the vector **x** contains the unknowns $\mathbf{u}'$, h', ρ' at the grid points. The matrix equation is solved using the standard routine EIG of the MATLAB (MATrix LABoratory) software to obtain all (σ, l) pairs.

To find **E** knowledge of the basic state is required. To this end, the function $\Theta(x)$ is defined by

$$\theta_r, \qquad x - x_m < -\frac{f_w}{2}$$

(Click the equation graphic to enlarge/reduce size)

and is used to represent both the basic-state upper-layer density and the layer thickness. Furthermore, $\alpha = 2\pi(x - x_m)/f_w$, θ_l and θ_r are the density and/or layer thickness values west and east of the front respectively, f_w is the width of the front, and x_m denotes the distance from the eastern wall to the middle of the front (see Fig. 3). For the jet to be free, it is required that $|x_m|$ is larger than the Rossby radius. In the application below, the Rossby radius is of $O(10)$ km, while the frontal area is located in the middle of a channel 100 km wide; that is, $x_m = -50$ km. Note that the basic state consists of eight variables, that is, the upper and lower layer alongchannel velocity components V_1 and V_2, the upper and lower layer densities R_1 and R_2, the upper and lower layer thicknesses H_1 and H_2, and the surface and interface deviations η and ζ. Since the variables are governed by (5) and (6) together with the relations (7) and (8), only five of them can be chosen independently. This point will be returned to in section 4.

3. Energetics

As suggested by McCreary et al. (1991), Fukamachi et al. (1995), and others (Holland 1978; Pinardi and Robinson 1986; Røed 1997) the nature and relative importance of the various instability processes are best understood by investigating the terms responsible for exchange, or conversion, of energy between the "mean" and the wave motion. Following McCreary et al. (1991) and Fukamachi et al. (1995), the mean motion is first defined as the average over one meridional wavelength $\lambda = 2\pi/l$; that is,

$$\langle q \rangle \equiv \frac{1}{\lambda} \int_y^{y+\lambda} q \, dy', \qquad (19)$$

where q is any of the model variables.

Next, kinetic and potential energy must be defined. Following the suggestion by Røed (1997), available gravitational energy (AGE) replaces the conventional potential energy. As indicated by its name, the source of the AGE is gravity and, equally important, it contains only that portion of the potential energy that is available for conversion into kinetic energy. AGE bears a strong resemblance to the available potential energy. However, in contrast to the available potential energy, it allows one to undertake a pointwise (in the horizontal) energy diagnosis. Let K denote the kinetic energy and Φ the AGE. Then, the total energy is defined by

$$\begin{aligned} E &= K + \Phi \\ &= \sum_{i=1}^{N} \left[\frac{1}{2}\rho_0 h_i \mathbf{u}_i^2 + \frac{1}{2} g(\varphi_i - \tilde{\varphi}_i)^2 + g h_i \sum_{j=1}^{i-1} \rho_j h_j - g\rho_i h_i D \right]. \end{aligned} \qquad (20)$$

Here the function $\varphi_i = \rho_i^{1/2} h_i$ and its reference value $\tilde{\varphi}_i = \tilde{\rho}_i^{1/2} \tilde{h}_i$, where the $(\sim)$ is used to denote a (constant) reference value of the variable in question, are introduced for convenience. Since both density and layer thicknesses may vary laterally in the basic state, the respective (constant) reference values are chosen to be equal their respective cross-channel average values; that is,

$$h_i = \frac{1}{L} \int_{-L}^{0} H_i(x) \, dx \qquad (21)$$

and

$$\tilde{\rho}_i = \frac{1}{h_i L} \int_{-L}^{0} H_i(x) R_i(x) \, dx. \qquad (22)$$

As is obvious, the first term on the right-hand side of (20) is the kinetic energy while the remaining terms constitute the AGE.

The average energy may be derived by substitution of (9)–(11) into (20) and then applying the operator (19). The result is

$$\langle E\rangle = \overline{E} + \langle E''\rangle, \quad (23)$$

where $\overline{E}$ is that part of energy that only involves $\langle q\rangle$ variables (henceforth the mean energy) and $\langle E''\rangle$ is the energy associated with the perturbation waves. As noted by several authors (e.g., McCreary et al. 1991) there is no unique way to decompose $\langle E\rangle$ into and $\langle E''\rangle$, and hence the division is ambiguous. Here the mean energy is chosen to consist of the basic-state variables only; that is,

$$\overline{E} = \sum_{i=1}^{N}\left[\frac{1}{2}\rho_0 H_i V_i^2 + \frac{1}{2}g(\overline{\varphi}_i - \tilde{\varphi}_i)^2 + gH_i\sum_{j=1}^{i-1}R_j H_j - gR_i H_i D\right], \quad (24)$$

where $\Phi_i = R^{1/2}{}_i H_i$. This is different from McCreary et al. (1991) who also included third-order correlations, that is, $O(\varepsilon^3)$ terms, in the definition of the mean. Here the focus is on the exchange of energy between the mean and the unstable waves, and the contributions of the $O(\varepsilon^3)$ terms are downplayed. The energy associated with the unstable waves becomes

$$\begin{aligned}\langle E''\rangle = {} & \sum_{i=1}^{N}\left[\frac{1}{2}\rho_0 H_i\langle u_i'^2 + v_i'^2\rangle + \rho_0 V_i\langle h_i' v_i'\rangle\right] \\ & + \sum_{i=1}^{N} g\left\{\left[R_i^{-1/2}\left(\overline{\varphi}_i - \frac{1}{2}\tilde{\varphi}_i\right) - D\right]\langle\rho_i' h_i'\rangle + \frac{1}{8}\tilde{\varphi}_i R_i^{-3/2} H_i\langle\rho_i'^2\rangle + \frac{1}{2}R_i\langle h_i'^2\rangle\right\} \\ & + \sum_{i=1}^{N}\sum_{j=i+1}^{N} g[H_j\langle\rho_i' h_i'\rangle + R_i\langle h_i' h_j'\rangle + H_i\langle\rho_j' h_j'\rangle] \end{aligned} \quad (25)$$

(Click the equation graphic to enlarge/reduce size)

and consists of second-order correlations only.

a. Energy budget equation

To investigate the relative importance of the various individual instabilities, an energy budget for the energy associated with the perturbations is required. To this end, (25) is first differentiated with respect to time. Next, all time derivatives of the perturbations are replaced making use of (12)–(14). In addition, (5) and (6) describing the basic state are used. The result is

$$\langle E''\rangle_t + P_x = C + S, \quad (26)$$

where P is a flux given by

$$P = \sum_{i=1}^{2} g(H_i R_i\langle h_i' u_i'\rangle + H_i^2\langle\rho_i' u_i'\rangle) + gH_1 H_2\langle\rho_1' u_2'\rangle + gR_1 H_2\langle h_1' u_2'\rangle + gR_1 H_1\langle h_2' u_1'\rangle \quad (27)$$

(Click the equation graphic to enlarge/reduce size)

and S is an energy dissipation term. The latter is found by collecting all the $\nabla^2(\ )$ terms; that is,

$$\begin{aligned} S = {} & \nu\rho_0\sum_{i=1}^{2}[H_i\langle\mathbf{u}_i'\cdot\nabla^2\mathbf{u}_i'\rangle + V_i\langle h_i'\nabla^2 v_i\rangle] + \nu g[\eta\langle h_1'\nabla^2\rho_1'\rangle + \zeta\langle h_2'\nabla^2\rho_2'\rangle + H_1\langle h_2'\nabla^2\rho_1'\rangle] \\ & + \nu g\sum_{i=1}^{2}\left[-\frac{1}{2}\tilde{\varphi}_i R_i^{-1/2}\langle h_i'\nabla^2\rho_i'\rangle + \frac{1}{4}\tilde{\varphi}_i R_i^{-3/2} H_i\langle\rho_i'\nabla^2\rho_i'\rangle\right]. \end{aligned} \quad (28)$$

(Click the equation graphic to enlarge/reduce size)

The remaining terms are lumped together in C as given by (29) below, which defines the energy conversion between the mean and eddy motions. It should be noted that from (25) and (17) it follows that $\langle E''\rangle_t = 2\sigma_i\langle E''\rangle$.

As alluded to above, the chosen mathematical formulation of C is ambiguous. In particular, the choice made for C

depends on the formulation chosen for the flux term P. The choice made here is based on the argument that both C and P should be recognizable in terms of known physical processes (Lorenz 1955; Harrison and Robinson 1978).

It is first noted that the chosen form (27) of P is recognizable as the pressure excess flux associated with the unstable waves (see Røed 1997). Second, to facilitate an interpretation of C, it is divided into three parts

$$C = C_1 + C_2 + C_3, \tag{29}$$

where

$$C_1 = -\rho_0 \sum_{i=1}^{N} H_i V_{ix} \langle u_i' \nu_i' \rangle - \rho_0 \sum_{i=1}^{N} V_i V_{ix} \langle h_i' u_i' \rangle - \rho_0 \sum_{i=1}^{N} H_i V_i \langle \nu_i' \nabla \cdot \mathbf{u}_i' \rangle, \tag{30}$$

$$C_2 = g(V_2 - V_1) R_1 \langle h_1' h_{2y}' \rangle - g\eta_x R_1 \langle h_1' u_1' \rangle - g(H_{1x} R_1 + \zeta_x R_2) \langle h_2' u_2' \rangle - \rho_0 \sum_{i=1}^{n} H_{ix} V_i \langle u_i' \nu_i' \rangle, \tag{31}$$

and

$$C_3 = C_{31} + C_{32} + C_{33}, \tag{32}$$

in which

$$C_{31} = -g\left(\eta - \frac{1}{2}\tilde{\varphi}_1 R_1^{-1/2}\right) R_{1x} \langle h_1' u_1' \rangle - g\left[H_1 R_{1x} + \zeta R_{2x} - \frac{1}{2}\tilde{\varphi}_2 R_2^{-1/2} R_{2x}\right] \langle h_2' u_2' \rangle + \sum_{i=1}^{N} \frac{1}{2} g \tilde{\varphi}_i H_i (R_i^{-1/2})_x \langle \rho_i' u_i' \rangle - \frac{1}{2} g \sum_{i=1}^{N} H_i V_i \langle h_i' \rho_{iy}' \rangle - g H_1 V_2 \langle h_2' \rho_{1y}' \rangle \tag{33}$$

$$C_{32} = g\left(-H_1 \zeta_x - \eta H_{1x} + \frac{1}{2}\tilde{\varphi}_1 R_1^{-1/2} H_{1x}\right) \langle \rho_1' u_1' \rangle + g\left(H_2 D_x - \zeta H_{2x} + \frac{1}{2}\tilde{\varphi}_2 R_2^{-1/2} H_{2x}\right) \langle \rho_2' u_2' \rangle \tag{34}$$

$$C_{33} = g\left(\frac{H_1^2}{2} - H_1 \eta + \frac{1}{2}\tilde{\varphi}_1 H_1 R_1^{-1/2}\right) \langle \rho_1' \nabla \cdot \mathbf{u}_1' \rangle + g\left(-\frac{H_2^2}{2} + H_2 D + \frac{1}{2}\tilde{\varphi}_2 H_2 R_2^{-1/2}\right) \langle \rho_2' \nabla \cdot \mathbf{u}_2' \rangle. \tag{35}$$

b. Discussion of the energy conversion

Inspection of (30) reveals that C_1 is proportional to the horizontal velocity shear. It is, therefore, associated with the kinetic energy exchange between the mean state and the unstable waves. As is common, it is recognized as the barotropic or the horizontal shear instability mechanism (Gill 1982). As displayed by (31), C_2 requires the presence of a vertical velocity shear combined with a thickness gradient in the basic state. It is, therefore, recognized as being a mixture of vertical shear instability and the conventional baroclinic instability mechanism. Hence, it will be referred to as a mixed vertical velocity shear and conventional baroclinic instability. Finally, the instability C_3 requires the presence of a horizontal density gradient and/or density fluctuations, and is thus recognized as the frontal instability as defined in the introduction. Among the terms in the frontal instability, C_{31} gets its energy from the mean across-channel density gradient and the alongchannel gradient in the density fluctuations. Here C_{32} is proportional to the layer thickness gradient of the basic state, while the term C_{33} is proportional to the gradient of horizontal velocity shear of the perturbation field. It is also noted that C_{32} contains terms proportional to bottom topography variations. Note that, if the model is reduced to a constant density layer model, then C_3 vanishes.

The above division of the conversion terms is different from that made by McCreary et al. (1991). They divided the energy conversion into four categories: barotropic, Kelvin–Helmholtz, frontal, and conventional baroclinic instability. In view of the ambiguity inherent in the choice of C, alternative ways of dividing the energy budget is likely to be a topic of further discussion.

Another item to consider is that the wave energy (25) includes expressions that can lead to negative energy. Therefore, a positive mean to perturbation energy conversion does not necessarily imply growth of an instability. Only if the conversion or pressure excess term flux is positively correlated with $\langle E'' \rangle_t$ will the wave amplitudes increase. Many former studies have already discussed this non-positive-definite perturbation energy (see Cairns 1979; Ripa 1983; Hayashi and Young 1987;Barth 1989ab; Fukamachi et al. 1995; Yu et al. 1995) and it is therefore not discussed further here.

4. Results of the linear stability analysis

Six cases are considered below (see Table 1); the first case is the reference run. Although it is constructed to yield a basic state similar to that used in the earlier studies, specifically those of Fukamachi et al. (1995), it is nevertheless significantly different due to the inclusion of the barotropic mode necessary to nullify the lower-layer velocity. It is therefore of interest in itself to investigate whether this has an effect upon the results of the earlier studies.

The remaining five cases are constructed to elucidate the effect on the instability of a combination of upper-layer thickness and density gradients (run 1), of variations in the horizontal mixing (run 2), of variations in the horizontal shear (width of the jet, run 3), of variations in the vertical velocity shear (run 4), and the presence of a sloping bottom (run 5). Note that, similar cases have been performed by McCreary et al. (1991) in a 2½-layer model (run 1), Fukamachi et al. (1995) in a 1½-layer model (runs 2 and 3), and Barth (1994) in a continuously stratified model (runs 4 and 5).

a. The reference run

In this case, the lower-layer velocity is set to zero and the lower-layer basic density is constant and equal to the reference density ρ_0. Then, (6) gives an expression for the sea surface elevation, and the upper-layer velocity is found by means of (5). Finally, it follows that

$$V_1 = -\frac{g}{\rho_0 f}\left[(\rho_0 - R_1)\zeta_x + \frac{1}{2}H_1 R_{1x}\right] \qquad (36)$$

and

$$\eta = \frac{R_{1l}}{R_1}\eta_l + \left(\frac{\rho_0 - R_{1l}}{R_1}\right)\zeta_l - \frac{(\rho_0 - R_1)}{R_1}\zeta, \qquad (37)$$

where the subscript l denotes the value of the variable in question at the western wall. Note that information of any slope in the equilibrium depth is hidden in ζ_x. If the bottom is flat, as assumed here, the actual constant value of the depth becomes redundant information. In this case, the initial conditions simulate essentially a reduced-gravity model. As shown by (36) and (37), only the depth of the interface may be chosen independently besides the upper- and lower-layer densities. Further, the interface is chosen to be flat, and a density front of width f_w = 40 km is located in the middle of a channel 100 km wide (Fig. 4). The associated frontal jet is southward (along the negative y axis) and has a maximum speed of 0.1 m s^{-1} (V_0 = −0.1 m s^{-1}). The central latitude of the channel is 41°N and hence the Coriolis parameter is $f = 1.1 \times 10^{-4}$ s^{-1}. The horizontal mixing coefficient is ν = 10 m^2 s^{-1}, and $R_2 = \rho_0$ = 1027.3 kg m^{-3}. In the upper layer, which contains the

front (Fig. 4), the lighter water of density 1026.3 kg m^{-3} is located west of the front, while the denser water (1026.8 kg m^{-3}) is located east of front. This gives a Rossby radius of approximately 8 km.

1) EIGENMODES

To resolve the frontal structure a grid mesh of size 1 km is chosen when solving the coupled eigenvalue equations as described in section 2c. The result is plotted in Fig. 5 and reveals that the unstable waves propagate in the direction of the basic-state current (negative phase speeds), but with a speed always less than the maximum jet speed. The fastest growing, or preferred, wave has a wavelength of approximately 15 km and an *e*-folding time (the reciprocal of σ_i) of 1.7 days (see the left panel of Fig. 5). It propagates with a phase speed of about $c_r = -0.09$ m s^{-1} that is, in the direction of the upper-layer jet and with 90% of its speed.

Inspection of Fig. 5 (left panel) also reveals that a bend of σ_i curve with wavelengths of about 60–70 km and *e*-folding times of about 5 days. These unstable waves propagate much slower and with a phase speed of −0.03 m s^{-1}, that is, in the direction of the jet with a speed of about one-third that of the short waves.

Details on the structure of the most unstable waves can be studied by inspection of Fig. 6. This figure has been constructed by plotting the variable

$$\Psi' = \sum_{j=1}^{M} \mathrm{Re}[\hat{\Psi}_j(x) e^{i(l_j y - \sigma_j t_0)}], \qquad (38)$$

where $\hat{\psi}_j(x)$, l_j, and σ_j represent the complex amplitude function, wavenumber, and complex frequency of the *j*th most unstable wave respectively, t_0 is an arbitrary nonzero time, and *M* is the total number of discrete alongfront wavenumbers chosen (here $M = 21$). Because the amplitudes of the wave fields must be of $O(\varepsilon)$ to satisfy the assumptions of a linearized model, they are scaled by choosing the maximum amplitude of the upper-layer density ρ'_1 to be 0.125 kg m^{-3}. The left panels of Fig. 6 show the total fields, that is, $\psi = \psi(x) + \psi'$, where $\psi(x)$ is the specified basic state.

As revealed by Fig. 6, the meander associated with the growing instability is evident in density, surface elevation, as well as the horizontal velocity fields. The alongchannel asymmetry is due to the different growth rates and phase speeds of the various unstable waves. Also the preference of the fastest growing short-wave instability is evident (right-hand panels of Fig. 6). The meandering current generated by the unstable waves advects cold saline coastal water offshore (to the west), which is compensated by advection of warm and fresh offshore water toward the coast (to the east). Moreover, Fig. 6 reveals that the mean density gradient across the front is weakened and that the surface deviation is much smaller than the interface deviation. The latter indicates that the unstable waves are dominantly baroclinic.

2) ENERGETICS

Regarding the shortest waves, the energy budget equation (26), as illustrated in Fig. 7, shows that the dominant balance is between $\langle E'' \rangle_t$ and *C*. Moreover, the energy transfer to unstable waves is confined to the area where the density gradient is close to its maximum value and thus seems to be uncorrelated with horizontal velocity shear. The energy dissipation term is negatively correlated to the perturbation energy, and hence the horizontal mixing opposes the formation of the unstable waves as expected. The energy flux gradient term is generally small and does not contribute significantly to the energy balance. As revealed by Fig. 7b, C_3 is by far the largest of the energy conversion terms. The barotropic term C_1 and the mixed conventional and vertical shear term C_2 are both very small. Hence, this unstable wave is driven by the available potential energy stored in the mean density gradient and the density and velocity fluctuations in the upper layer. To distinguish it from the conventional geostrophic baroclinic instability, Barth (1989a,b; 1994) referred to this kind of instability as ageostrophic instability. Here, these short unstable waves will simply be referred to as the “frontal waves” or the “frontal mode.”

A similar energy analysis for the long-wave instability reveals that the balance between $\langle E'' \rangle_t$ and *C* still dominates (see Fig. 8). The energy conversion now encompasses the whole region over which the basic state varies. Furthermore, it has a two-peak structure with the peaks located exactly where the horizontal velocity shear is maximum. This indicates that the longer unstable waves are related to the horizontal velocity shear. Indeed, although the frontal instability C_3 still dominates, energy conversion due to the barotropic instability process represented by C_1 cannot be ignored. Again both the diffusion and pressure excess flux terms are small, with diffusion opposing the energy conversion.

Although the long-wave instability is primarily frontal too for the reference run, it can be shown later that barotropic instability becomes more important when the lateral density gradient is decreased or the horizontal velocity shear is increased. These long unstable waves will therefore be referred to as “mixed waves” or the“mixed mode.”

b. The effect of an upper-layer density gradient combined with an interface deviation (run 1)

As revealed by (36), the basic-state jet of the reference run may equally well be produced by a setup in which the upper-layer density gradient is reduced, and the interface deviation is given a compensating gradient ($R_{1x} \neq 0$ and $\zeta_x \neq 0$). Indeed, the upper-layer jet may be reproduced even with $R_{1x} = 0$.

1) EIGENMODES

A typical case in which both $R_{1x} \neq 0$ and $\zeta_x \neq 0$ is shown in Fig. 9. The growth rate and phase speed for this case is plotted in Fig. 10 (dashed line). For comparison the corresponding curves for the reference run are plotted in the same figure (solid line).

Inspection of Fig. 10a shows that the growth rate is decreased for all wavelengths compared to the reference run. While the phase speeds for the long unstable waves decrease, the phase speeds for the short unstable waves (see Fig. 10b) increase.

To verify that the small-scale instability waves are indeed due to the frontal instability, the above procedure was repeated with $R_{1x} = 0$, in which case the model is reduced to a conventional, constant density layer model, in that no density perturbations are allowed ($\rho'_1 = 0$). Thus, the basic-state jet is balanced by the gradient of the upper-layer thickness only as given by (36). In this case, the growth rate associated with the fastest growing unstable wave is about 8.5 days and is hence greatly decreased compared to the previous model (see the dash–dot curve in Fig. 10a). Moreover, all the waves shorter than 40 km are no longer unstable. In fact, the fastest growing wave has a wavelength of about 70 km associated with a phase speed of about 0.02 m s^{-1} (see dash–dot curve in Fig. 10b); that is, the wavelength is unchanged, while the phase speed has been reduced compared to the mixed wave of the reference run. The diminishing importance of the frontal instability wave, when the lateral density gradient is decreased, supports the previous finding that the frontal wave is indeed caused by the lateral density gradient, that is, by the presence of the front.

2) ENERGETICS

The energy budget for the frontal wave is very similar to the reference run and is therefore not shown. The frontal instability term C_3 is the only conversion term that is positively correlated to $\langle E'' \rangle_t$, with the mixed conventional and vertical shear instability C_2 being negatively correlated to $\langle E'' \rangle_t$ and thus tending to weaken the instability.

Regarding the mixed mode (long wavelength) instability, the energy flux gradient term $-P_x$ is now significant and is positively correlated with $\langle E'' \rangle_t$ outside of the central frontal area (Fig. 11). In the central area, the energy flux term combined with the energy conversion term C balance $\langle E'' \rangle_t$. The energy flux advects energy into the central part of the frontal area and helps to increase the energy of the unstable waves, while it advects energy from the two sides of the central area and hence decreases the energy of the unstable waves there. As displayed by Fig. 11b, all the conversion terms are important to the long unstable waves. As expected, the importance of the barotropic instability conversion C_1 is limited to the areas where the velocity shear is maximum and is insignificant in the central area where the frontal instability conversion term C_3 dominates. Curiously, the mixed conventional–vertical shear conversion C_2 is important only on the inshore (eastern) side of the front where the velocity shear is maximum, approaching the magnitude of the barotropic instability conversion term C_1. In conclusion, the preferred long unstable wave mode is caused by a mixture of barotropic and baroclinic instability.

c. Effects due to horizontal mixing (run 2)

In this case, the horizontal mixing coefficient ν was varied from 0 to 50 $m^2\ s^{-1}$ in steps of 5 $m^2\ s^{-1}$ (see run 2, Table 1), and the eigenvalue problem solved for each of the 11 values. The result is shown in Fig. 12. The effect on the frontal wave is to increase its wavelength from 15 to 30 km (look at Fig. 12a). However, the wavelength of the preferred long-wave instability appears to be unaffected and is nearly constant and equal to 70 km. Furthermore, it is found that the phase speed of the unstable waves are almost independent of the horizontal mixing coefficient (not shown). This is in line with Fukamachi et al. (1995) and serves to show that the effect of the barotropic mode is insignificant.

Figure 12b shows that the maximum growth rate of the frontal mode monotonically decreases as ν increases and that it has dropped by a factor of 2 when the horizontal mixing coefficient is increased from 10 to 50 $m^2\ s^{-1}$. As $\nu \rightarrow 0$, the wavelength of the preferred frontal mode goes to zero. Thus, the introduction of viscosity helps to give a preferred finite wavelength for the frontal mode. In this connection it is interesting to note that Young and Chen (1995) found that the introduction of a weak vertical density stratification within the mixed layer has a similar effect.

Finally, as revealed by Fig. 12b, the maximum growth rate of the long-wave instability or the mixed mode (look at the dotted line) decreases only slightly as the horizontal mixing coefficient ν increases. Additionally, it is observed that the mixed

mode always has a growth rate smaller than the frontal mode. The energy analysis corroborates the findings above and is, therefore, not shown.

Thus, independently of the value chosen for the horizontal mixing the preferred short wave is always associated with the frontal instability and the preferred long wave with the mixed mode instability.

d. Effects due to a varying horizontal shear (run 3)

Because the structure of a front varies from season to season and from one geographical area to the next, the influence of a varying width of the front is also of some interest. This is illustrated in Fig. 13, where the width of the front is varied from 10 to 60 km in steps of 5 km (see Table 1, run 3). It should be noted that when the maximum speed is kept constant at 0.1 m s^{-1}, an increase (decrease) in the width of the front corresponds to a decrease (increase) in the horizontal shear.

1) EIGENMODES

As revealed by Fig. 13a, the wavelength corresponding to the frontal wave increases slightly from 13 to 16 km as the front width increases from 20 to 60 km. The wavelength of the fastest growing mixed mode also increases with increasing wavelength. The slope of the dotted line relative to the dashed implies that the wavelength of the fastest growing mixed mode undergoes larger variations than the fastest growing frontal mode.

It should be noted that the importance of the mixed mode in terms of the growth rate increases as the width of the front decreases. This is illustrated in Fig. 13b, which shows that the growth rate of the frontal wave increases nearly logarithmic with increasing front width, that is, the wider the front the faster the growth rate, while the mixed wave experiences a near linear decrease. In fact, the two lines intersect at the point $f_w = f_c = 20.6$ km. At this point, the frontal and mixed wave have the same growth rate (*e*-folding time about 3.8 days). When $f_w < f_c$, the mixed wave dominates, whereas the frontal wave dominates when $f_w > f_c$, indicating that the relative importance of the mixed wave increases with increasing shear.

Another feature of the frontal wave is that it develops only when the front is wider than 15 km. The mixed mode, on the other hand, forms a preferred band only when the front width is less than 40 km, an indication that when the horizontal shear decreases (increasing frontal width) the mixed mode ceases to exist as a predominant unstable wave.

These results are valid for an eddy viscosity of $\nu = 10$ m^2 s^{-1}. It is therefore of interest to investigate if this is the case for other values of eddy viscosity. To this end, a series of calculations for different eddy viscosities and frontal widths are performed. The result is plotted in Fig. 14. The shaded region corresponds to the region where the frontal instability wave ceases to exist. Thus, the relative importance of the frontal instability wave diminishes when the front becomes narrower for all values of the viscosity coefficient ν. Figure 14 also reveals that the frontal instability wave grows faster when the front is wide and the eddy viscosity is low. Moreover, the growth rate is more sensitive to variations in the horizontal viscosity when the front is wider.

Finally, it is noted that the phase speed decreases for all waves when the horizontal shear increases, and this effect is more pronounced in the long wavelength band than in the short wavelength band (not shown).

2) ENERGETICS

While the energy analysis for the frontal mode reveals no major change over the reference run when the front width is varied, this is not the case for the mixed mode. When the frontal width is narrowed to 20 km, the energy flux gradient term $-P_x$ is significant and positively correlated to the perturbation energy outside of the central front area (e.g., $|x| > 60$ km and $|x| < 40$ km), all other contributions to (26) being negligibly small there (Fig. 15b). This indicates that the energy change outside the central area is purely caused by an energy flux away from the frontal area. In contrast, the energy flux is negatively correlated with the energy change within the central area and thus acts to oppose the conversion of energy there. As expected, the barotropic instability C_1 dominates in the area of large horizontal velocity shear and is positively correlated with $\langle E'' \rangle_t$ there. In the area of maximum velocity (and hence little shear), C_1 drops to zero and the frontal instability C_3 dominates. Thus, as the front narrows the long-wave instability becomes a truly mixed barotropic–frontal instability.

e. Effects due to vertical velocity shear (run 4)

In many upwelling situations, the upper-layer jet is accompanied by an opposite jet in the lower layer. This situation is simulated here by specifying a basic state in which a sloping interface and a lower-layer density variation are introduced in combination with surface elevation and upper-layer density gradients. The resulting basic state is shown in Fig. 16, in which the lower-layer jet is opposite to the upper-layer jet, and with only a slightly lower speed ($V_{02} = 0.08$ m s^{-1}). Thus,

the vertical shear has been increased by 80% compared to the reference run (see Table 1, run 4). Note that this case is somewhat similar to run 1 in that both a lateral density gradient and an interface gradient are included (see Figs. 16 and 9). Note also that, when the constraint of a motionless lower layer is relaxed, (36) is no longer valid and the surface elevation η must be specified independently of R_1 and ζ. Finally, note that a slight lateral density gradient in the lower layer has been imposed as well.

1) EIGENMODES

As revealed by Fig. 17, the introduction of the lower-layer jet gives an increased growth rate for all wavelengths. This is particularly true for the fastest growing short wave, which experiences an increase of ~ 30% (from 1.7 days to about 1.3 days) at a slightly shorter wavelength. It is also observed that the mixed mode no longer forms a preferred band. The magnitude of the phase speed is slightly reduced for all wavelengths. This conclusion is hardly surprising. It supports the earlier findings of Ikeda and Apel (1981), who used a quasigeostrophic model to show that the addition of a jet in the lower layer in the same direction as the upper-layer jet, that is, a reduced vertical velocity shear weakens the baroclinic instability. A similar conclusion was also reached by Barth (1994), who used a continuously stratified model. Thus, an increased vertical shear acts to enhance the baroclinic instability.

2) ENERGETICS

As shown in Fig. 18, the conversion term C still balances the $\langle E'' \rangle_t$ term for the short wavelength instability. The frontal instability term C_3 is the only conversion term that is positively correlated to $\langle E'' \rangle_t$, and hence the only contributor to instability amplification. The mixed conventional and vertical shear instability term C_2 is negatively correlated to $\langle E'' \rangle_t$ and thus tends to weaken the instability.

Since there is no clear preferred band of long unstable waves (Fig. 17), the energy budget analysis for the long waves is not shown here.

f. The effect of bottom topography (run 5)

Finally, the effect of a linear bottom topography is investigated. The setup chosen is as close to run 4 as possible with a linear bottom slope of -2×10^3 (see Table 1, run 5). The results may, therefore, be compared with the results of run 4. The linear stability analysis reveals that a sloping bottom only slightly reduces the growth rate of the frontal mode and that its phase speed is not influenced. The phase speed of the mixed mode is slightly reduced (not shown).

Thus, it is concluded that the frontal instabilities are trapped in the upper layer and that, in a coastal upwelling region over a (moderately) sloping shelf, the unstable modes appear not to be significantly affected by a variable bottom topography.

5. Comparison with results derived from a numerical model experiment

Experiments with numerical models have shown that waves similar to those revealed by the analysis above may be produced in upwelling areas both with an idealized straight coast (McCreary et al. 1991; Stevens et al. 1997) and with realistic coastline geometry and bathymetry (Røed 1996). The above experiments investigated wind-driven upwelling fronts close to the coast, that is, with a continuous frontogenesis associated with the favorable upwelling wind conditions. The associated frontal jet is, therefore, too close to the coast for the jet to be considered free. It is therefore of some interest to perform an idealized numerical experiment with a free jet and to compare it with the analysis above. To this end, the 1½-layer model of Røed (1996) is used to perform a corresponding numerical experiment because, as shown, the effect of the barotropic mode is insignificant. The model solves the primitive equations in spherical coordinate (for details, see Røed 1995, 1996). Because of the spherical coordinates, the channel has been rotated 90° to fit the cyclic boundary conditions employed at the open ends of the channel. A channel 419 km long and 280 km wide is used, which with a grid size of 1.39 km gives 301 × 201 grid points. Initially, a front 40 km wide is located in the middle of the domain with a maximum velocity of −0.1 m s^{-1}. Thus, both the front and the Rossby radius are well resolved. Since the walls are far removed from the front, the effect of the side walls can be neglected. The initial condition mimics the basic state of the reference run (shown in Fig. 4). To trigger the instability, this geostropically balanced jet is perturbed with ten geostropically balanced waves of random phases at the initial time. The summed amplitudes of the perturbations are maximum 10% of the initial background field. The model is then allowed to progress in time without further interference. In this run no entrainment/detrainment is allowed and no forcing is applied; that is, the governing equations are essentially those given by (1)–(3).

Figure 19 shows the results in terms of the Fourier transform constructed from the density structure along the middle of the front after 8 and 10 days, respectively. The dominant wave lengths are centered on 14 km in both cases, while the peak energy increases from 0.0566×10^3 to 0.2240×10^3 kg^2 m^{-5}, an increase of about $e^{1.3}$ within two days. This entails that the e-folding time for the dominant wave is approximately 1.5 days. Thus, both the preferred wavelength band and the growth rate are consistent with the frontal wave predicted by the linear stability analysis of the reference run.

Figures 20a,b show the structure of the density and the density anomaly after 10 days and may be compared with those shown in Figs. 6a,b. The density anomaly field is obtained by subtracting the background structure from the basic-state density field so that the wavelengths of the unstable modes become distinguishable. The results are qualitatively similar

to the numerical solution that evolved from a free jet in Fukamachi (1992) at the early stage of the development. They also clearly support the earlier findings that, when linear effects dominate, small-scale instabilities with wavelengths of about 14 km form upon the front and that these instabilities are frontally trapped.

The correlation between the linear model and the early stage of the numerical model is striking. Even the U-shaped structure of the unstable waves (compare Fig. 6b with Fig. 20b) is captured by the numerical model. The alongchannel asymmetry is also evident in the model results.

At a later stage, small eddies form (Figs. 20c,d). At this stage, a weakly nonlinear effect starts, and the dominant wavelengths are now increased to about 30 km. Later, at t = 80 days, the nonlinear effect completely dominates the picture in that large-scale eddies and filaments appear over most of the domain. The basic-state front structure no longer exists because the amplitudes of the distortions are comparable to those of the basic state. Figure 20f shows that the scale of the filaments is between 80 and 120 km and the local density gradient is intensified by the eddies and filaments.

Further inspection of the time evolution of the Fourier transforms at the middle of the front (Fig. 21) shows that the dominant wave (about 14 km) appears first (t = 10 days) in accordance with the linear stability theory. At t = 24 days, the dominant central wavelength increases to about 30 km. As time progresses, the majority of the wave energy moves to even longer waves; for example, at t = 55 days the energy spectrum shows a single peak at 45 km. Later the energy accumulates at 80 km and with less energy distributed in the shorter wavelength band. At t = 100 days, there is significant energy on a broad band between 90 and 150 km where the filaments appear. It is of interest to note that the scale increase of disturbances in the present experiment is qualitatively similar to that of the forced solution of McCreary et al. (1991) in a 2½-layer model. The progression of wave energy from shorter to longer waves is an indication that the instabilities exemplify a process which is “upgradient.” It cannot therefore be parameterized by a simple “downgradient” diffusion parameterization, and hence underscores the point made by Visbeck et al. (1997).

6. Summary and conclusions

A linear stability study of a two-layer, finite-depth, primitive equation model is presented. It extends the analyses of Barth (1994), Fukamachi et al. (1995), and Young and Chen (1995) in several ways. First, the effects of a variable across-front bottom topography, frontal (nonlinear) variations in the interface and surface elevations, and two opposing jets in the two layers (increased vertical shear) are investigated. The present model also allows density gradients and density fluctuations in the lower layer as well as in the upper layer.

The energy analysis departs from the earlier studies in that the available gravitational energy replaces the conventional potential energy. Additionally, a different choice is made in separating the terms that define conversion of energy from the basic state to the unstable wave state. The combination of these changes leads to a different interpretation of the instability mechanisms, yet leaves their relative importance intact.

Six cases are considered, of which the first is a reference run. The other five are sensitivity analyses. Through these six cases, a portion of the parameter space not previously mapped out is presented, which serves to reinforce the earlier conclusions.

A reference run is first performed in which the basic state consists of an upper-layer jet only and thus mimics the set up considered by Fukamachi et al. (1995). The results of this case are very much in line with the results of Fukamachi et al. (1995), who used a reduced-gravity version of the model. The results of the reference run show that the effect of the barotropic mode on the preferred instability waves is not significant. Thus, two prominent bands of unstable waves are found, with the frontal mode having growth rates (e-folding times) typically of order 1–2 days. The mixed mode, on the other hand, typically gives maximum growth rates of about 3–5 days, that is, a much slower growth.

The results of the reference run are verified against results derived using a numerical model. The model employed is a 1½-layer model similar to that utilized by McCreary et al. (1991) and Røed (1996). In the initial stage, the model features a geostrophically balanced jet in the middle of a zonal channel. This initial balanced state is then perturbed. No other energy dissipative mechanism is involved. The regular unstable waves that develop at the front in the numerical model are indeed quite similar to the unstable waves predicted by the linear stability theory both qualitatively and quantitatively. This is gratifying and supports the hypothesis that the small-scale waves observed in frontal areas are indeed caused by the presence of the front.

In all cases considered and in line with the earlier studies, it is found that the unstable waves propagate in the direction of the basic-state jet with phase speeds invariably less than the basic jet speed. In addition, the phase speeds of different frontal modes is only slightly less than the jet speed, while the mixed mode moves with a speed about one-third of that of the frontal mode. The existence of two preferred bands of unstable waves of different growth rates and phase speeds leads to an apparent asymmetry along the direction of the jet in the regular wave train, with areas of stronger wave activity in regions where the two modes interact positively. This conspicuous asymmetry is also reproduced by the numerical model.

Except for two special cases, it is found that the frontal mode dominates the mixed mode based on the observed relative difference in the growth rates. One of the exceptional cases is discovered when the relative importance of the surface elevation and the lateral density gradients are varied in constructing a given upper-layer jet. By systematically lessening the intensity of the front, it is found that the importance of the frontal mode is progressively diminished. Indeed, when the front vanishes (no upper-layer lateral density gradient), the frontal mode ceases to exist. Interestingly, during this process the

mixed mode is unchanged in wavelength, growth rate, and phase speed.

The second case in which the importance of the frontal mode is diminished is discovered by increasing the horizontal velocity shear in the jet. The shear is increased simply by decreasing the width of the front while keeping the maximum jet speed constant. In fact, as the width of the front is decreased to a certain critical value, the two modes become equally important (see Fig. 13). When the width is decreased beyond this point, the frontal mode becomes less important. Interestingly, this is the case for all values of the eddy viscosity (except for zero viscosity in which case the frontal mode wavelength goes to zero). This is not the case for the mixed mode which continues to increase in growth rate as the front narrows.

It is found that the inclusion of horizontal viscosity is essential to form a preferred frontal mode band of unstable waves that have a finite wavelength. In this regard, it is interesting to note that Young and Chen (1995) found that the inclusion of a slight vertical density gradient has the same effect.

Perhaps the single most important conclusion of the present study is that, except in the single extreme case mentioned above, one expects a separate band of small-scale unstable waves of wavelengths on the order of 10–30 km to form at any front. These waves, which exist regardless of the model used (whether finite depth or reduced gravity), are trapped in the upper layer and owe their existence to the presence of a lateral density gradient.

Acknowledgments

This study was supported by the Research Council of Norway (NFR) through Contract 109227/110 and in part by the MORENA (Multidisciplinary Oceanographic Research in the Eastern Boundary of the North Atlantic) project under the European Union MAST II program (Contract MAS2-CT93-0065). We would like to thank Anders Rudberg for the coding of the multilayer version of OSMOM. Useful discussions with Bruce Hackett and Arne Melsom at DNMI are greatly appreciated. Our appreciation goes also to two anonymous reviewers and Julian P. McCreary whose constructive criticisms have helped to improve this work.

REFERENCES

Barth, J. A., 1989a: Stability of a coastal upwelling front: 1, Model development and a stability theorem. *J. Geophys. Res.*, **94,** 10 844–10 856..

— ,1989b: Stability of a coastal upwelling front: 2, Model results and comparison with observations. *J. Geophys. Res.*, **94,** 10 857–10 883..

— ,1994: Short-wavelength instabilities on coastal jets and fronts. *J. Geophys. Res.*, **99,** 16 095–16 115..

Cairns, R. A., 1979: The role of negative energy in some instabilities of parallel flows. *J. Fluid. Mech.*, **92,** 1–14..

Feliks, Y., and M. Ghil, 1993: Downwelling–front instability and eddy formation in the eastern Mediterranean. *J. Phys. Oceanogr.*, **23,** 61–78.. Find this article online

Fukamachi, Y., 1992: Instability of density fronts in layer and continuously stratified models. Ph.D. thesis, Nova University, 166 pp..

— ,J. P. McCreary, and J. A. Proehl, 1995: Instability of density fronts in layer and continuously stratified models. *J. Geophys. Res.*, **100,** 2559–2577..

Gill, A. E., 1982: *Atmosphere–Ocean Dynamics.* Academic Press, 662 pp..

Haidvogel, D. B., J. L. Wilkin, and R. E. Young, 1991: A semispectral primitive equation ocean circulation model using vertical sigma and orthogonal curvilinear horizontal coordinates. *J. Comput. Phys.*, **94,** 151–185.

Harrison, D. E., and A. R. Robinson, 1978: Energy analysis of open ocean regions of turbulent flows—Mean eddy energetics of a numerical ocean circulation experiment. *Dyn. Atmos. Oceans*, **2,** 185–211..

Hayashi, Y.-Y., and W. R. Young, 1987: Stable and unstable shear modes of rotating parallel flows in shallow water. *J. Fluid Mech.*, **184,** 477–540..

Haynes, R., E. D. Barton, and I. Pilling, 1993: Development, persistence, and variability of upwelling filaments off the Atlantic Coast of the Iberian Peninsula. *J. Geophys. Res.*, **98,** 22 681–22 692..

Holland, W. R., 1978: The role of mesoscale eddies in the general circulation of the ocean—Numerical experiments using a wind-driven quasi-geostrophic model. *J. Phys. Oceanogr.*, **8,** 363–392.. Find this article online

Hoskins, B. J., 1974: The role of potential vorticity in symmetric stability and instability. *Quart. J. Roy. Meteor. Soc.*, **100,** 480–482..

Ikeda, M., and J. R. Apel, 1981: Mesoscale eddies detached from spatially growing meanders in an eastward-flowing oceanic jet using a

two-layer quasi-geostrophic model. *J. Phys. Oceanogr.*, **11,** 1638–1661.. Find this article online

Lee, S.-K., and G. T. Csanady, 1994: Instability waves in the gulf stream front and its thermocline layer. *J. Mar. Res.*, **52,** 837–863..

Lorenz, E. N., 1955: Available potential energy and the maintenance of the general circulation. *Tellus,* **7,** 157–167..

McCreary J. P., Y. Fukamachi, and P. K. Kundu, 1991: A numerical investigation of jets and eddies near an eastern ocean boundary. *J. Geophys. Res.*, **96,** 2515–2534..

Phillips, N., 1954: Energy transformations and meridional circulations associated with simple baroclinic waves in a two-layer model. *Tellus,* **6,** 273–280..

Pinardi, N., and A. R. Robinson, 1986: Quasigeostrophic energetics of open ocean regions. *Dyn. Atmos. Oceans,* **10,** 185–219..

Ripa, P., 1983: General stability conditions from zonal flows in the one-layer model on the β-plane or the sphere. *J. Fluid Mech.,* **126,** 463–487..

Røed, L. P., 1995: Documentation of the Oslo Multilayer Mesoscale Ocean Model-OSMOM. Part 1: The governing equations. DNMI Research Report Series No. 24, ISNN 0332-9879, Norwegian Meteorological Institute (DNMI), Oslo, Norway, 23 pp..

— ~~,~~1996: Modeling mesoscale features in the ocean. *Waves and Nonlinear Processes in Hydrodynamics,* J. Grue, B. Gjevik, and J. E. Weber, Eds., Kluwer Academic, 383–396..

— ~~,~~1997: Energy diagnostics in a 1½-layer, non-isopycnic model. *J. Phys. Oceanogr.,* **27,** 1472–1476.. Find this article online

Sousa, F. M., 1995: Mesoscale processes off the Portuguese coast using satellite data and *in situ* data. Ph.D. dissertation, University of Lisbon, 167 pp..

Stevens, I. G., J. J. Johnson, L. P. Røed, X. B. Shi, P. T. Jacobs, and P. A. Davis, 1997: Final intermodel comparisons trials. MORENA Sci. Tech. Rep. No. 40, University of Lisbon, Lisbon, Portugal, 16 pp..

Visbeck, M., J. Marshall, and T. Haine, 1997: Specification of eddy transfer coefficients in coarse-resolution ocean circulation models. *J. Phys. Oceanogr.*, **27,** 381–402.. Find this article online

Young, W. R., 1994: The subinertial mixed layer approximation. *J. Phys. Oceanogr.*, **24,** 1812–1816.. Find this article online

— ~~,~~and L. Chen, 1995: Baroclinic instability and thermohaline gradient alignment in the mixed layer. *J. Phys. Oceanogr.*, **25,** 3172–3185.. Find this article online

Yu, Z., J. P. McCreary, and J. A. Proehl, 1995: Meridional asymmetry and energetics of tropical instability waves. *J. Phys. Oceanogr.*, **25,** 2997–3007.. Find this article online

---

Tables

Table 1. The parameters used in the different cases: V_{01} and V_{02} are the maximum jet speeds in the upper and lower layers, respectively, f_w is the front width, ν is the horizontal viscosity, ζ is the interface elevation, and R_1 is the upper-layer density, and $D_x \equiv (D_e - D_w)/L$ is the bottom slope, where D_e and D_w are the water depth near the eastern and western walls, respectively. The notation 10(5)60 means that the variable in question is varied from 10 to 60 units in steps of five units.

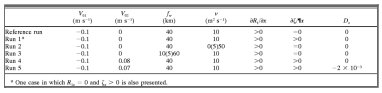

Click on thumbnail for full-sized image.

Figures

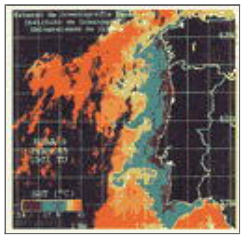

Click on thumbnail for full-sized image.

Fig. 1. *NOAA-14* satellite image showing sea surface temperature off the Iberian Peninsula 26 September 1995, that is, toward the end of the upwelling season. Note the cold upwelled water along the coast and the superimposed small-scale instability

waves of wavelengths 15–30 km. Note also the longer-scale filaments positioned at 41° and 42°N bringing cold water offshore. (Courtesy of A. G. F. Fiúza, University of Lisbon.)

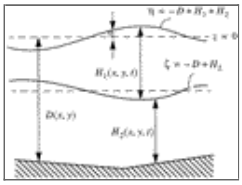

Click on thumbnail for full-sized image.

Fig. 2. Sketch of the layering structure for a two-active layer, finite-depth model conveniently showing the notation used in the text.

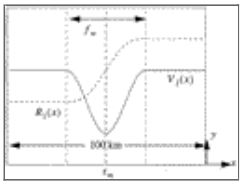

Click on thumbnail for full-sized image.

Fig. 3. Sketch of the basic state variables for the reference run. The fine dashed line gives the density distribution, while the solid line gives the upper-layer velocity as calculated from (5). Dash–dot lines are used to indicate the free jet area according to (18). Note that the figure is not drawn to scale.

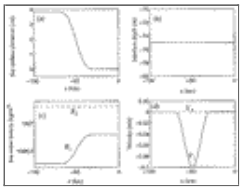

Click on thumbnail for full-sized image.

Fig. 4. Solid (dashed) lines show upper (lower) layer basic-state variables of the reference run as functions of the cross-channel distance: (a) the surface elevation (in cm) (b) the interface depth in meters (flat), (c) the density (in kg m^{-3}, and (d) the velocity. Cross-channel distance in kilometers is shown along the horizontal axis.

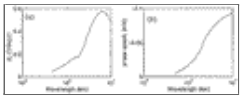

Click on thumbnail for full-sized image.

Fig. 5. Solid curve show the growth rates (left panel) and phase speeds (right panel) as functions of wavelength for the reference run (see Table 1). The wavelength scale shown along the horizontal axis is logarithmic and decreases to the right, along the vertical axis of the left-hand panel is shown the growth rate in day^{-1}, while the vertical axis of the right panel shows the phase speed (in m s^{-1}).

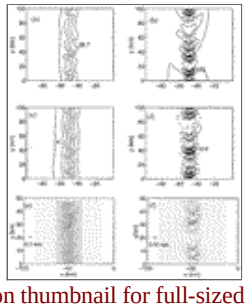

Click on thumbnail for full-sized image.

Fig. 6. Along- and cross-channel structure of the instabilities for the most unstable waves as constructed from (38). Only the upper-layer variables are shown. Solid and dashed lines in panels (b) and (d) represent positive and negative amplitudes, respectively: (a) the density (contour interval 0.1 kg m^{-3}), (b) the density anomaly (contour interval 0.025 kg m^{-3}). (c) the surface deviation (in cm: contour interval 0.5 cm), (d) the interface deviation (anomaly) (in m: contour interval 1 m), (e) the velocity field, including the basic-state jet for the upper layer, and (f) the perturbation velocity. Note that the scale along the *y* axis in panels (e) and (f) is half shown in the remaining panels. The numbers appearing in panel (b) and (d) are maximum values.

Click on thumbnail for full-sized image.

Fig. 7. Cross-channel variation of the various terms entering the energy budget equation (26) for the short, fast growing wave of the reference run: (a) the four terms concerned (26). Note that the energy exchange term (dash–dot curve) nearly balances the time rate of change of the perturbation energy (solid line) everywhere, and that the energy flux term (dotted curve) and the diffusion term (dashed curve) are both small. (b) The three terms (30)–(32) contributing to the energy conversion of (a). Of the three, the frontal instability is by far the largest.

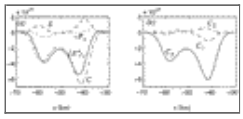

Click on thumbnail for full-sized image.

Fig. 8. As in Fig. 7 but for the longer and slower growing unstable wave (mixed mode) of the reference run.

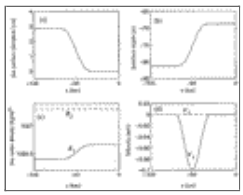

Click on thumbnail for full-sized image.

Fig. 9. As in Fig. 4 but for run 1 (see Table 1). Note the decreased lateral density gradient in the upper layer.

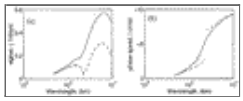

Click on thumbnail for full-sized image.

Fig. 10. As in Fig. 5 but showing the growth rates and phase speeds of the reference run (solid line) and run 1 (dashed and dash–dot curves), respectively. Note that the growth rate increases for all wavelengths compared to the reference run and that the phase speeds are diminished for long unstable waves and increased for short unstable waves. The dash–dot lines show the growth rate and phase speed of a constant density layer model ($R_{1x} = 0, \rho'_1 = 0$), while the dashed curve is for the basic state shown in Fig. 9.

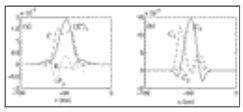

Click on thumbnail for full-sized image.

Fig. 11. As in Fig. 8 except for run 1 for which the basic state is illustrated in Fig. 9 (see Table 1).

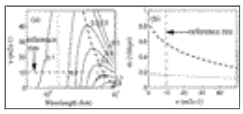

Click on thumbnail for full-sized image.

Fig. 12. (a) Contours (solid curves) of growth rates as function of horizontal viscosity and wavelength for the most unstable waves for run 2 (see Table 1). The dashed and dotted lines represent the wavelength associated with maximum growth rate and are replotted in (b) as a function of the horizontal viscosity. Values corresponding to the reference run are shown by the dash–dot line for comparison.

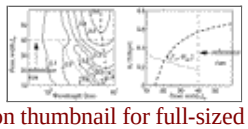

Click on thumbnail for full-sized image.

Fig. 13. As in Fig. 12 but for run 3 (see Table 1). (a: left) Contours (solid curves) of growth rates as function of front width and wavelength for the most unstable waves. Note that the two curves of (b: right) intersect for a front width f_c about 20 km. In this case, the long-wave and short-wave instability are of equal importance (equally preferred).

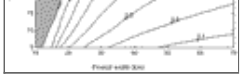

Click on thumbnail for full-sized image.

Fig. 14. The contour lines show the growth rate (day^{-1}) of the most unstable frontal wave as a function of front width x_w and viscosity coefficient ν. There is no frontal instability wave in the shaded area. The frontal wave develops only when the front is wider than 15 km at ν = 10.

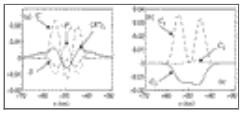

Click on thumbnail for full-sized image.

Fig. 15. As in Fig. 8 but for run 3 (see Table 1) when the frontal width is 20 km. Note that C_1 peaks exactly where the basic-state jet has its maximum shear and is positively correlated with E_t there.

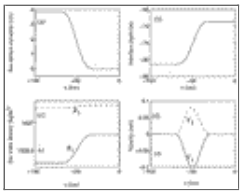

Click on thumbnail for full-sized image.

Fig. 16. As in Fig. 4 but for run 4 (see Table 1). Note that the introduction of a basic-state jet in the lower layer opposite to the upper-layer jet.

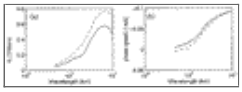

Click on thumbnail for full-sized image.

Fig. 17. As in Fig. 10 but for run 4. The dashed curves correspond to run 4, while the solid curves show the reference run. Note that the growth rate increases with increasing vertical shear for all wavelengths. The phase speeds are all diminished, in particular for the longer unstable waves.

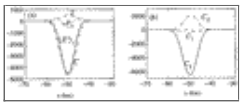

Click on thumbnail for full-sized image.

Fig. 18. As in Fig. 7 except for the case with increased vertical shear (see Table 1, run 4, and Fig. 16).

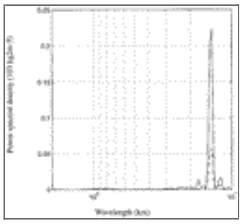

Click on thumbnail for full-sized image.

Fig. 19. The Fourier transform along the middle of front. The sold and dashed lines represent t = 10 days and t = 8 days, respectively.

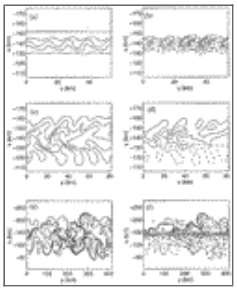

Click on thumbnail for full-sized image.

Fig. 20. The three left-hand panels show the density of model simulation, while the three right-hand panels show the density anomalies in the upper layer as function of along- and cross-channel coordinates. Panels (a) and (b) are at t = 10 days, (c) and (d) are at t = 24 days, and (e) and (f) are at t = 80 days. Positive and negative amplitudes are presented by solid and dashed lines, respectively. In (a)–(d) only a small representative area is shown, while the full channel area is shown in (e) and (f).

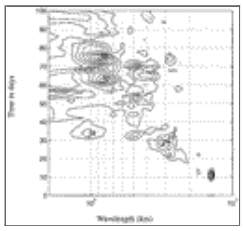

Click on thumbnail for full-sized image.

Fig. 21. Time evolution of the wavenumber spectrum derived from the density field. The result are derived by taking a Fourier transform along the middle of the front. Contour intervals are 5 $kg^2\ m^{-5}$.

Additional affiliation: University of Oslo, Oslo, Norway.

Corresponding author address: Lars Petter Røed, Norwegian Meteorological Institute, P.O. Box 43 Blindern, N-0313 Oslo, Norway.

E-mail: larspetter.roed@dnmi.no

top